Enhanced electrochemical activity of boron-doped nanocarbon functionalized reticulated vitreous carbon structures for water treatment applications

Iwona Kaczmarzyk [a], Mariusz Banasiak [a], Paweł Jakóbczyk [a,g], Michał Sobaszek [a,*],
Gabriel Strugała [c], Tomasz Seramak [d], Paweł Rostkowski [e], Jakub Karczewski [a,b],
Mirosław Sawczak [f], Jacek Ryl [a,b], Robert Bogdanowicz [a,b]

[a] Gdansk University of Technology, Narutowicza 11/12, 80-233 Gdansk, Poland
[b] Advanced Materials Centre, Gdańsk University of Technology, 80-233 Gdansk, Poland
[c] Department of Materials Science and Technology, Institute of Manufacturing and Materials Technology, Faculty of Mechanical Engineering and Ship Technology, Gdańsk University of Technology, 80-233 Gdańsk, Poland
[d] Department of Manufacturing and Production Engineering, Institute of Manufacturing and Materials Technology, Faculty of Mechanical Engineering and Ship Technology, Gdańsk University of Technology, 80-233 Gdańsk, Poland
[e] The Climate and Environmental Research Institute NILU, Instituttveien 18, 2007, Kjeller, Norway
[f] The Szewalski Institute of Fluid-Flow Machinery, Polish Academy of Sciences, Fiszera 14, 80-231 Gdansk, Poland
[g] Institute of Biotechnology and Molecular Medicine, Kampinoska 25, 80-180 Gdansk, Poland

ARTICLE INFO

ABSTRACT

An extraordinary charge transfer kinetics and chemical stability make a boron-doped diamond (BDD) a promising material for electrochemical applications including wastewater treatment. Yet, with flat geometrical surfaces its scaling options are limited. In this study, the reticulated Vitreous Carbon (RVC) served as a substrate for boron-doped diamondized nanocarbons (BDNC) film growth resulting with complex heterogeneity carbon structures with different morphologies defined by using electron microscopy, microtomography, activation energy studies, and Raman spectroscopy.

The proposed modification significantly boosted the electrochemical $Fe(CN)_6^{3-/4-}$ redox activity. The voltammetry and impedimetric studies revealed its origin as a significantly higher share of electrochemically active sites at the BDNC@RVC electrode (increased by 114 %) combined with enhanced heterogeneous rate constant ($2\times$ increase up to $8.24\cdot10^{-4}$ cm s^{-1}). Finally, to establish its applicability for water treatment, the BDNC@RVC was studied as the anode in electrochemical paracetamol decomposition. Boron-enriched nanoarchitecture formed at the RVC electrode surface substantially reduced the oxidation energy barrier manifested as a decrease in activation overpotential by 212 mV, which gave a consequence in a 78 % removal rate (in 4 h, at 0.7 mA cm^{-2}), 12 % higher than bare RVC and yielding lower amounts of APAP decomposition intermediates.

1. Introduction

Reticulated vitreous carbon (RVC) has aroused scientists' interest worldwide as a commercially available microporous, glassy carbon (GC) electrode material. RVC is an open-pore vitreous carbon foam material of honeycomb structure [1–4]. RVC has a wide range of applications [5], such as: batteries [6], redox flow batteries [7], microbial fuel cells [8,9], removal of metal ions [10,11], electrochemical wastewater treatment [12–15], electrochemical oxidation of dyes [16,17] and phenols [18].

RVC is useful electrode material, it has an exceptionally high void volume, well-developed surface area, high porosities, high electrical conductivity, low resistance to fluid flow, chemical stability, and inertness over a wide range of bases and acids [,20]. However, the skeletal structure of the material is breakable and due to the low volumetric carbon content, a uniform potential- and current distribution through the material is not assured.

RVC surfaces can be easily surface modified in many ways, including enzymes, biochemical species, organic coatings, metals, metal oxides,

---

* Corresponding author.
  E-mail address: micsobas@pg.edu.pl (M. Sobaszek).

composites, and carbon nanomaterials [6,7,9,16,21–26]. The surface modifications of RVC electrodes enhance mechanical properties and improve the efficiency of electrochemical processes [20], which expanded their usage and applications. Due to the variety of modifications, RVC could be used as cost-effective, efficient, and environmentally friendly electrode materials for water treatment. RVC as three-dimensional electrodes overcome mass transport limitation, caused by low concentrations of organic compounds in the aqueous matrices. In addition, the open pores structures generate flow turbulence. It leads to a significant increase in the mass transfer coefficient, which in turn produces greater current efficiencies and lower energy consumption. Moreover, the developed surface of the RVC electrode strongly improves on electrode oxidation process. Valdez et al. studied the degradation of paracetamol (APAP) on modified reticulated vitreous carbon electrodes with layers of TiO_2 and $CuO/TiO_2/Al_2O_3$ [27]. Moreover, it compared three different processes to degrade APAP: the photochemical process, the electrochemical process, and the photoelectrochemical process. For electrolysis carried out with $CuO/TiO_2/Al_2O_3/RVC$ electrode, 98 % APAP degradation took 1 h, for non-modified RVC electrode, 90 % degradation was achieved in 4 h. In comparison, Brillas et al. reported 91 % APAP removal by electrochemical oxidation processes by the time 4 h for standard BDD electrode [28].

Millan-Barba et al. demonstrated a growth and electrical characterization of boron-doped diamond over porous carbon fibre (CF) from microwave plasma enhanced chemical vapor deposition MP-CVD [29]. Micrographs reveal two extreme type layers dependent on growth conditions. Some of CF was completely covered by boron-doped diamond (BDD), however, the diamond coating is not uniform and varies in thickness by the length of the fibre. On the other side, they show that carbon nanowalls are formed on the interlayer of CF instead of BDD. Extensive 3D structure causes problems with uniform diamond formation, moreover, the RVC turbostratic and its disordered level may affect the diamond growth. However, the mechanisms of carbon by-product formation are not fully understood. Diamond RVC composites should be considered as a new 3D form with variable surface texture and conductivity, depending on the depth of the analyzed plane. Diniz et al. analyze and discuss diamond morphologies on three-dimensional RVC surface using hot filament CVD [30]. The inner region of diamond/RVC composites show the lower thickness of nanocrystalline diamond film considering of poor concentration of atomic hydrogen and consequently lower growth rate on deeper regions. Micrographs show agglomerates, which may be attributed to the secondary nucleation process when the top layer was uniform cover by microcrystalline diamond film [30]. Moreover, grown microcrystalline diamond film is related to heat treatment temperature [31].

Boron-doped diamond films as an electrode material exhibit excellent electrical carrier mobility up to 400 $cm^2V^{-1} s^{-1}$ [32,33]. The carbon-based layer allows for advanced oxidation processes [34,35] utilizing organic pollutants [36,37] more efficiently. The recent use of BDD electrodes tends to be very effective in the decomposition of different organic pollutants including PFOA and PFOS [38], ionic liquids [32], phenol [39], and dyes [40,41], which originates from the intrinsic BDD feature of lower activation overpotentials during direct oxidation but efficacy in hydroxyl radicals formation [42–44]. Relatively easy manufacturing on various substrates via a chemical vapor deposition system [45–49] makes this material a superior candidate as the modification of RVC improves its electrical parameters while preserving high specific surface and low fluid flow resistance. The structure and electrochemical properties of boron-doped diamond electrodes depend on factors such as the boron doping concentration, surface termination, and interactions of superficial non-diamond phases [50–53]. Moreover, BDD layers are well known for they mechanical, chemical [54,55] and thermal stability [56], corrosion [57] and biofouling resistance [58], with might be very attractive for wastewater electrolysis. These features are particularly important considering the control of contaminants degradation routes on homogeneous surfaces. Overall, it may be recognized

that surface modification of RVC substrates with BDD films constitutes an attractive route to tailor electrodes with features such as high charge transfer kinetics and environmental stability, preferred under electrochemical oxidation conditions. Further research proved high electric double-layer capacitance [59–61], increased current density [62], and enhanced photoelectrochemical properties [63] of the porous BDD electrode.

Non-diamond sp^2 states are the primary charge transfer mediators resulting in higher electrochemical activity. The composite BDD with graphite electrodes improved charge electron transfer for other-sphere and inner-sphere redox probe [64]. Nanoarchitectured carbon material designed and synthesized by Pierpaoli et al. comprising vertically aligned boron-doped graphene walls grown on a BDD interfacial layer significantly increased the electrochemically active sites, improving the exchange current density [65]. The designed composite has a peculiar maze-like morphology and a higher surface area. It's worth noting that the highly developed surface area like in the case of boron-doped graphene walls suggests an enhanced efficiency towards the degradation of various pollutants.

This work aims to present and understand the charge transfer enhancement of the commercially available RVC materials through the boron doped diamondized nanocarbons (BDNC) which consist of boron-doped diamond, carbon nanowalls/boron-doped diamond and graphitic layers, fabricated by CVD, to increase electrode electrochemical activity. The electrochemical evaluation of the modified RVC electrode including the heterogeneous rate constant (k^0), and voltammetric peak-to-peak separation values for the $Fe(CN)_6^{3-/4-}$ redox process was shown, concluding that the BDNC layers grown on the RVC foams lead to the development of electrochemically-active surface morphology and interfacial electron transfer kinetics. The proposed electrode modification by the BDNC structures allowed for the electrode to be successfully utilized for electrolytic degradation of acetaminophen. Characterizing highly developed electrochemical active surface favorable the Faradaic reactions. Potentially, the achieved results could be adapted also to hazardous pollutant groups.

2. Experimental

2.1. Materials

Duocel ® RVC (type: 30 PPI, 3 % relative density) from ERG Aerospace Corporation was used for all of the experiments called here as RVC. Sodium sulphate ($\geq$99 %, anhydrous, ACS reagent), potassium ferricyanide $K_3[Fe(CN)_6]$ ($\geq$99 %, anhydrous, ACS reagent) and $K_4[Fe(CN)_6]$ ($\geq$99 %, anhydrous, ACS reagent) were used to preparation of aqueous solutions based on demineralized water. Paracetamol (European Pharmacopoeia (EP) Reference Standard) was purchased from Sigma-Aldrich.

2.2. Preparation of the BDNC@RVC electrode

BDNC film was deposited using the optimized parameters of BDD layer growth in a microwave plasma-enhanced chemical vapor deposition (MPCVD) system (SEKI Technotron AX5400S, Japan) on an RVC substrate ($20 \times 20 \times 5$ mm). The substrate was seeded in water-based nanodiamond suspension of 4 nm NDs (Nano Ando, Japan) through deep coating. Next, substrates were carefully dried in a stream of nitrogen. The heated stage temperature was set to 700 °C, microwave radiation power to 1300 W, and process pressure to 50 Torr. The gas composition consisted of 1 % of CH_4: H_2, and diborane (B_2H_6) precursor ([B]/[C] of 10,000 ppm in the gas phase). The growth time was set to 4 h.

2.3. Characterization of the BDNC@RVC electrodes

2.3.1. SEM

The morphology of the samples was investigated by Scanning

Electron Microscope (SEM). Images were obtained using FE-SEM Quanta FEG 250 (FEI) with an ET secondary electron detector using 20 kV accelerating voltage.

2.3.2. μCT

The computed microtomography (μCT) of samples was performed using GE phoenix v|tome|xs. The x-ray power was set at 30 W (100 kV, 300 μA). The exposure time for each radiogram was set at 5000 ms. The voxel resolution was 26.55 μm. A total of 1000 radiographs were made per full rotation of the sample. 3D reconstructions were performed using phoenix datos/2 software using a standard reconstruction algorithm. The commercial package VGStudio Max was used to analyze the porosity of the samples. For this purpose, an arbitrary volume was set up to represent only the region of interest (ROI - the volume of the cuboid inside each sample). The thresholding algorithm in VGStudio Max 2.2 software was used to calculate the porosity. The porosity calculation of the sample was the ratio of pore volume to ROI volume (solid material volume + pore volume).

2.3.3. Raman spectroscopy

Raman spectra were recorded at room temperature using a micro-Raman spectrometer (Invia, Renishaw) equipped with a 514 nm Ar$^+$ laser and 50× microscope objective. To avoid sample heating the radiation power was set below 2 mW while the laser spot diameter on the sample surface was about 2 μm. The spectral resolution was better than 2 cm^{-1}. Each sample was analyzed at five randomly selected points and each spectrum was averaged from five measurements. The spectra were recorded on the cross-section of the sample at different distances from the top surface (depth level in Fig. 3). In addition, a reference spectrum of the uncoated RVC substrate was recorded on the underside of the sample.

2.3.4. Electrochemical measurements

The electrochemical measurements were done using a potentiostat-galvanostat (VMP-300, Bio-Logic, France), controlled by EC-Lab software. Cyclic voltammetry (CV) and electrochemical impedance spectroscopy (EIS) were carried out in a three-electrode setup with the RVC and BDNC@RVC as the working electrode, Ag/AgCl/3.0 M KCl as the reference electrode and platinum net as the counter electrode. The geometric surface area of the electrode immersed in the electrolyte A = 9.6 and 7.8 cm^2 for RVC and BDNC@RVC, respectively. Determination of the surface modification efficiency was based on CV studies in 0.25 M Na$_2$SO$_4$ with 2.5 mM [Fe(CN)$_6$]$^{4-/3-}$ chosen as the redox probe. Before the electrochemical measurements, the solutions were deoxygenated with argon. The CV experiments were done at a scan rate of 5–1000 mV s^{-1} and the potential range was from −0.5 to 1.0 V vs. Ag/AgCl/3.0 M KCl. The EIS experiment was carried out at open circuit potential (OCP), with voltage perturbation amplitude of 10 mV, and in the frequency range of $1 \cdot 10^5$ to $1 \cdot 10^{-2}$ Hz, 10 points per frequency decade. All measurements were recorded at a constant temperature of 25 °C.

The standard heterogeneous rate constant k^0 was estimated from the CV studies at a scan rate of 10 mV s^{-1}, using the Nicholson approach for quasi-reversible one-electron transfer, with Eq. (1):

$$k^0 = \psi \cdot \sqrt{\frac{\pi \cdot D \cdot \nu \cdot F \cdot n}{R \cdot T}} \tag{1}$$

where ψ is the dimensionless kinetic parameter estimated from literature based on peak potential separation ΔE_P [66], D_0 is the diffusion coefficient of [Fe(CN)$_6$]$^{3-/4-}$ (6.67 10^{-6} cm^{2}s^{-1}), n is the number of electrons transferred, ν is the applied scan rate (Vs^{-1}), R corresponds to gas constant (8.314 J K^{-1} mol^{-1}), F is the Faraday's constant (96,485C mol^{-1}) and T is the temperature (298 K).

The electrochemically active surface area (EASA), A_e (cm^2) was determined through the commonly used modified Randles-Sevcik equation for a non-reversible, one-step, one-electron reaction (2) [67].

$$i_p = 2.99 \cdot 10^5 \cdot n \cdot \alpha^{\frac{3}{2}} \cdot A \cdot \nu^{\frac{1}{2}} \cdot D_0^{\frac{1}{2}} \cdot c_0 \tag{2}$$

where i_p is peak current (A), c_0 is the concentration of the diffusing species (mol dm^{-3}), D_0 is the diffusion coefficient (6.67·10^{-6} cm^2 s^{-1}), ν is the scan rate (V s^{-1}), and α is transfer coefficient, estimated as 0.5. The $i_p = f(\nu^{1/2})$ characteristics of each studied surface are presented in Fig. 7C and D.

2.3.5. Orbitrap mass spectrometry analyses

Ultra-high performance liquid chromatography (UHPLC- model Vanquish Horizon) coupled with ultra-high-resolution mass spectrometer Orbitrap Q-Exactive-Plus (both from ThermoFisher Scientific) were used to analyze APAP and its transformation products. The mass spectrometer was equipped with a heated electrospray ion source (HESI) that was operated in negative and in positive mode. Chromatographic separation in negative mode was achieved on a Waters® Acquity HSS T3 (100 Å, 1.8 μm, 150 × 2.1 mm) a gradient of pure water (A) and methanol (B) and with a gradient of 0.1 % formic acid in water (A) and acetonitrile (B). The acquisition was carried out in a full scan and data-dependent acquisition (top5) mode to facilitate the identification of products and their confirmation. The injection was 2 μL.

2.4. Electrochemical oxidation setup

A solution of 100 g L^{-1} of APAP in methanol was prepared for degradation via electrolysis studies. Then an aliquot volume of the standard stock solution was added to the 0.1 M Na$_2$SO$_4$ to obtain 200 mg L^{-1} of APAP. The electrochemical oxidation process was carried out in galvanostatic conditions at 0.7 mA cm^{-2} in a two-electrode system. The electrolysis system consists of a glass beaker, anode, and platinum net cathode. Potentiostat-galvanostat VMP-300 Bio-Logic (France) and EC-Lab software were used. The electrolysis process was carried out under ambient conditions (25 °C) for 240 min with continuous stirring by a magnetic stirrer.

3. Results and discussion

3.1. Structural and morphological characterizations

The application of boron-doped nanocarbon layers onto substrates with complex morphologies, such as porous RVC (Reticulated Vitreous Carbon) foam, is not a standard procedure [68]. Fig. 1A presents an SEM (Scanning Electron Microscopy) micrograph of the uncoated RVC foam, while Fig. 1B, C, and D display the resulting topographical variations at different depths within the foam structure. Fig. 1E explains the orientation of the RVC in relation to the plasma, also indicating the specific positioning within the foam's architecture. As evidenced in Fig. 1B, the side facing the plasma acquires a typical polycrystalline boron-doped diamond (BDD) layer. The RVC's uppermost surface is completely encapsulated by the BDD, as confirmed by the characteristic Raman peak at 480 cm^{-1} shown in Fig. 2A (top spectrum). Diamond crystals have been formed with an average size of approximately 300 nm. This grain size significantly influences the electrical transport properties, with a notable effect on carrier mobility and resistivity due to the proliferation of grain boundaries that can impede electrical conductivity.

Deeper within the RVC structure, layers are coated with boron-doped nanocarbons (BDNC), which exhibit a nanowall-like topography and reveal diamondized properties through an intense D band in their Raman spectra. Progressing further to the stage-face side of the foam, the observed topography transitions to a degenerated, undulating carbon nanowall structure, which is enriched with graphitic phases. This is evidenced in the Raman spectra by a pronounced attenuation of the D band and a heightened intensity of the G band.

The intricate effect depicted in Fig. 1 can be ascribed to several key factors. Initially, there is the complicated architecture of the RVC foam,
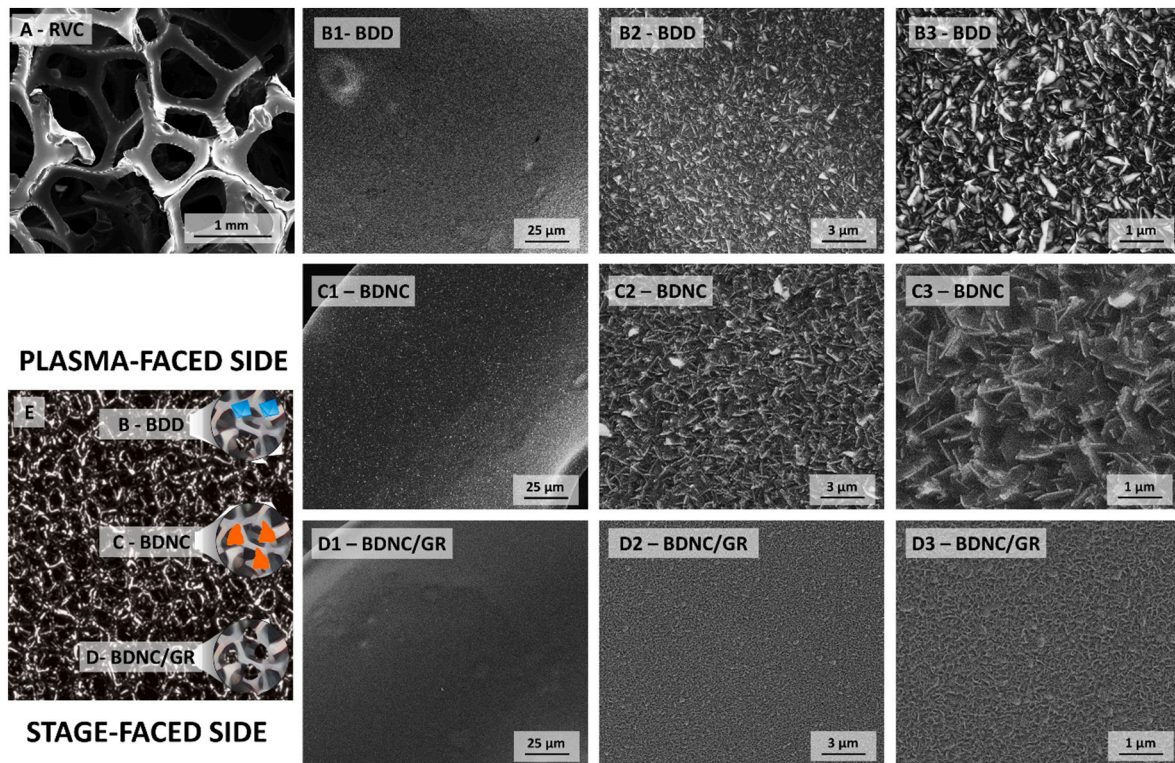
Fig. 1. SEM micrograph of A) bare RVC foam, B) plasma-faced side of RVC foam covered by boron-doped diamond-rich (BDD) nanocarbons, C) intermediate section of RVC foam covered by boron-doped nanocarbons (BDNC) with nanowalls-like topography, D) stage-faced side covered by boron-doped nanocarbon/graphitic film, and E) schematic representation of B), C) and D) on RVC anode.
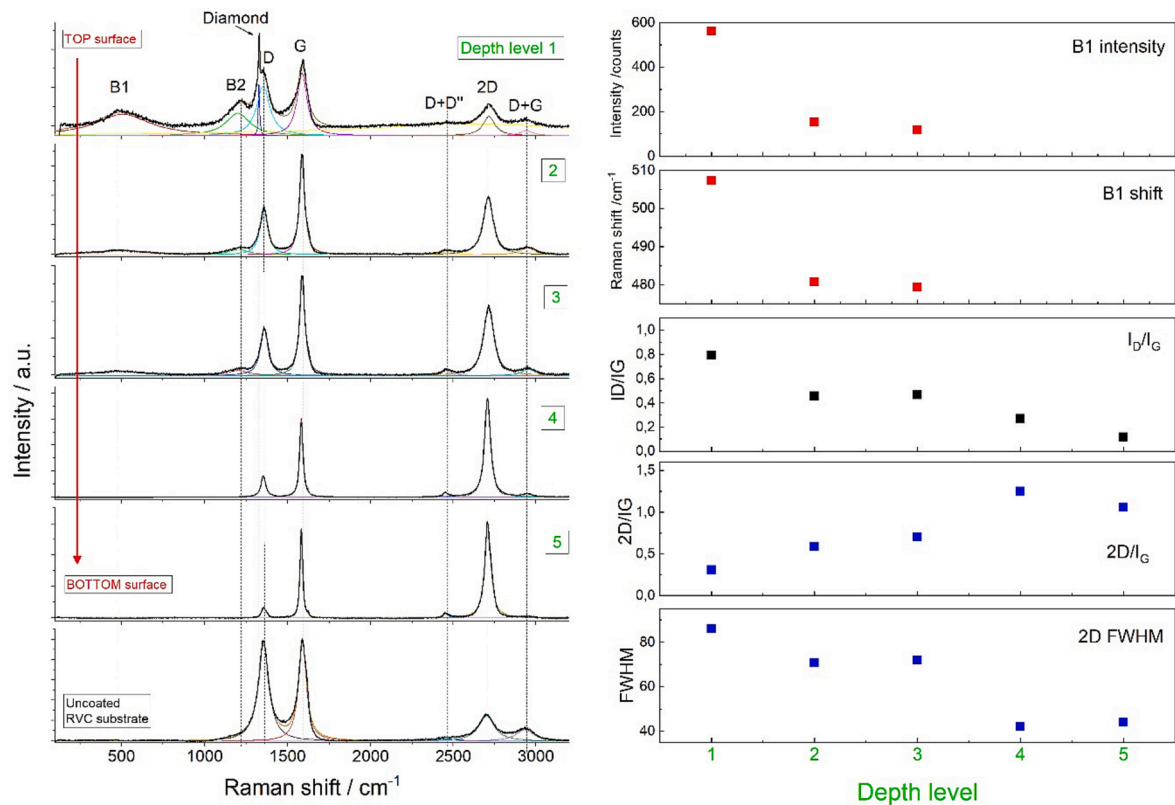

Fig. 2. A) Evolution of Raman spectra on a cross-section of an RVC substrate coated with BDNC, B) the change of the peaks and FWHM.

which boasts a considerable thickness of approximately 5 mm and is seated upon a molybdenum stage. This configuration presents challenges for the effective transmission of microwave plasma throughout the foam, resulting in a vertical gradient of both microwave power density and local surface temperature. Moreover, as the distance increases from the microwave plasma source and approaches the shim, there is a notable accumulation of recombined carbon species. This phenomenon concurrently diminishes the power delivered to the system, leading to the formation of defected non-diamond nanocarbon phases [69]. Typically, such nanocarbon structures develop when the carbon carrier concentration is significantly high, often exceeding 1 %, for instance at levels around 8 % [40,70].

Fig. 2A shows the evolution of Raman spectra measured for RVC substrate with deposited BDNC nanostructures. The bare RVC is characterized by two major bands, namely disorder-induced dispersive D-band (1357 cm^{-1}) corresponding to the breathing modes of sp^2 coordinated defective graphitic phases. By the side of, the graphite G-band (1597 cm^{-1}), assigned to the sp^2 C—C stretching E_{2g} mode [38]. Next, the overtone bands attributed to D + D″, 2D and D + G bands are located in the range of 2400–3000 cm^{-1}.

With a change in depth, a clear difference in the structure of the coating can be observed. Raman spectra recorded on the upper surface contains bands characteristic of boron-doped diamond (BDD) coexisting with an sp^2 graphite-like phase. The narrow intense zone center optical phonon band (ZCP) of the diamond centered at 1327.5 cm^{-1} is redshifted vs diamond line (1332.5 cm^{-1}) due to the Fano effect resulting from interaction between discrete diamond zone-center phonon and electronic Raman scattering effects [71]. This band is assisted with two wide bands located near 507 cm^{-1} (B1) and 1200 cm^{-1} (B2) that can be attributed to vibration modes of boron atoms allocated in diamond lattice [71,72]. The diamond line fades quickly with increasing depth, while bands B1 and B2 are still visible in deeper layers and their intensity slowly decreases with depth. With a decrease in the intensity of the B1 and B2 bands, a redshift of the B1 band is also observed, which is associated with a change in the boron concentration [72]. As the depth increases, the sp^2 phase Raman band structure also changes. There is a clear difference in the relative intensity of the D and G bands, in addition, a redshift and increase in the intensity of the 2D band centered near 2700 cm^{-1} is observed. The evolution of the band structure may be assigned to the change in the crystalline structure of the graphene-like nanomaterial. Due to the three-dimensional structure of the substrate and its electrical properties, the plasma field penetration depth during the CVD process is limited, as a result of which a gradient is observed in the coating structure. At smaller depths, the Raman band structure corresponds to multilayer graphene, while at greater depths, the Raman spectrum is characteristic of a single-layer graphene-like nanomaterial [73]. The Raman spectrum of the RVC substrate is characteristic of glassy carbon-like structures, with D and G bands located at 1354 and 1588 cm^{-1}, respectively. In addition, overtones are observed in the region of 2500–3500 cm^{-1}. The position, intensity and width of Raman bands for spectra recorded at different depths (compare Fig. 2A) are collected in Table 1.

The determination of the real porosity of unmodified and modified RVC structures is problematic due to the brittleness of the carbon ribs and three-dimensional porosity. A method that is perfectly suitable for these purposes due to its non-destructive nature is computed micro-tomography. The virtual 3D reconstruction provides a comprehensive structural analysis including the determination of the degree of porosity [74–77].

The results of the 3D reconstructions, including magnifications of the structures of both samples of bare RVC foam and after BDNC deposition are shown in Fig. 3A and D. The analysis of these structures showed that diamond deposition reduced the roughness of the ribs. The same reconstructions were used in the volumetric porosity calculations. The visual three-dimensional results of the porosity calculations are based on graphs presented in Fig. 3B and E, which also demonstrate three-

Table 1
Position (ω), intensity (A) and width (FWHM) of Raman bands recorded at different depths of RVC coated substrate.

Depth lvl	1			2			3			4			5			6		
	ω	A	FWHM	ω	A	FWHM	ω	A	FWHM	ω	A	FWHM	ω	A	FWHM	ω	A	FWHM
B1	507.20	562.03	399.92	480.67	150.85	360.71	479.30	116.35	381.86	X	X	X	X	X	X	X	X	X
B2	1199.79	588.84	174.44	1203.67	179.92	145.08	1202.66	142.85	144.28	X	X	X	X	X	X	X	X	X
ZCP	1327.54	1337.65	9.18	X	X	X	X	X	X	X	X	X	X	X	X	X	X	X
D	1352.63	1297.28	96.00	1356.43	1535.26	56.04	1358.67	1264.22	55.56	1353.44	826.56	34.23	1356.59	334.35	35.29	1354.48	4792.67	79.15
G	1586.37	1641.85	70.81	1586.50	3369.21	37.55	1587.35	2722.07	38.53	1582.01	3055.01	23.53	1581.90	2852.98	19.36	1588.58	4948.58	56.83
D + D″	2612.40	305.64	1763.65	2460.02	120.06	102.41	2459.75	133.62	68.84	2454.48	166.94	40.87	2456.10	145.30	40.58	2463.51	114.39	178.04
2D	2716.40	505.81	86.07	2712.24	1970.14	70.62	2714.57	1897.10	71.81	2707.65	3821.26	41.90	2709.51	3014.13	43.93	2701.66	1247.84	116.10
D + G	2940.39	128.43	100.35	2949.53	223.75	105.86	2953.99	171.94	91.29	2948.92	116.55	70.25	2955.20	43.77	46.42	2931.52	572.76	130.05
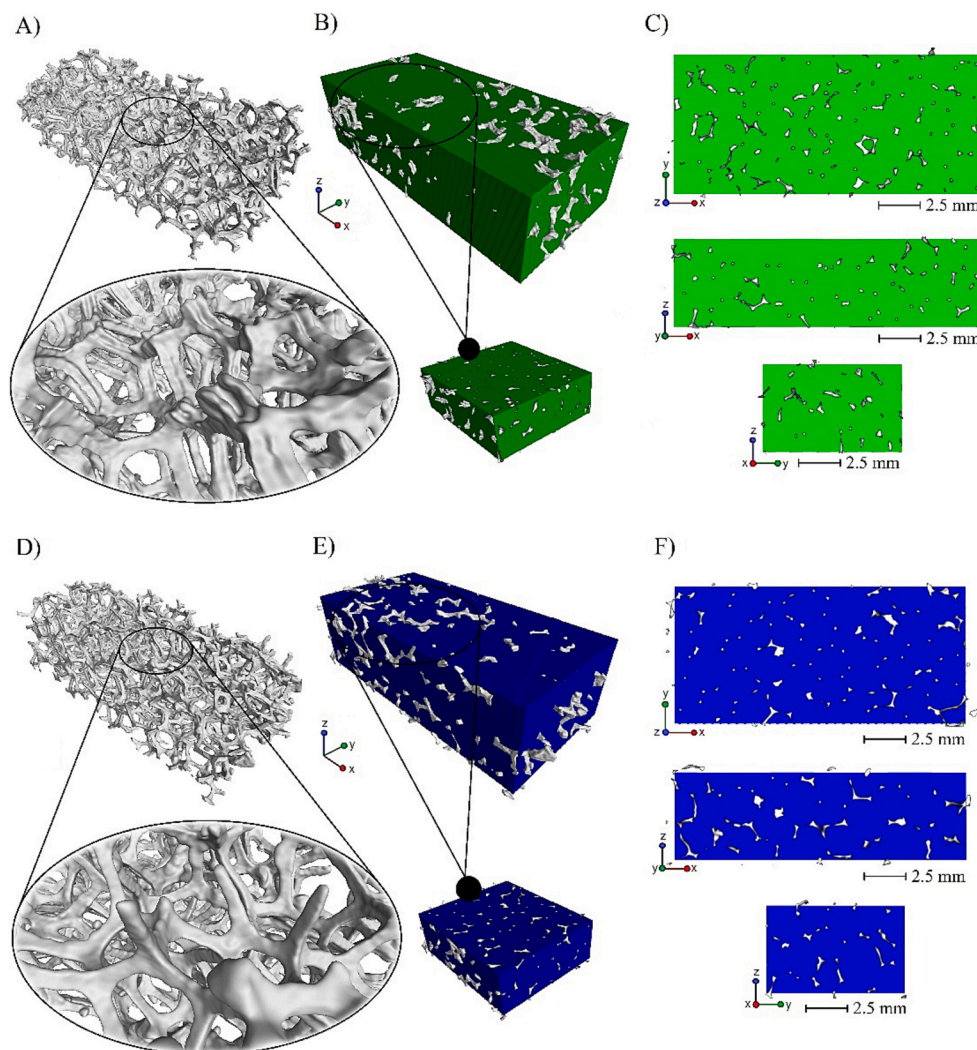
Fig. 3. Microtomography of bare RVC (A, B, C) and BDNC@RVC (D, E, F); A) and D) 3D reconstruction with magnification of the rib structure; B) and E) 3D visual representation of the volumetric calculation of porosity with cross-section of two cutting planes (XY, YZ); C) and F) 2-dimensional cross-sections with porosity calculations in the central section of the sample with XY, XZ, YZ cutting planes.

dimensionally the porosity inside the samples. Fig. 3C and F show two-dimensional cross-sections of 3D reconstructed samples to provide the cross-section of the ribs and to show the visual comparison of the porosity. A comparison of the cross-sectional images reveals that the cross-sections of ribs in the modified sample were less uniform in terms of thickness than the ribs in the reference sample. Furthermore, the full numerical calculations of the porosity of the samples are shown in Table 2. Calculated in ROI, the volume porosity of the reference sample was 93.19 %, while the volume porosity of the BDNC@RVC was 93.57 %. On the other hand, the percentage of surface porosity was 66.96 % and 68.77 % for bare RVC and BDNC@RVC, respectively. Notably, the modification affected the rib structure and this translated into increased porosity.

Electrical measurements were performed by creating two ohmic contacts between opposite sides of the RVC electrode, thus measuring the material by volume along one dimension. Such a method is a reliable source of resistance measurements for porous materials [78,79]. Resistance of unmodified RVC electrode and BDNC-modified from measurements along horizontal directions are similar to each other (RVC 74 Ω vs BDNC@RVC 63 Ω) revealing high conductivity of deposited BDNC. Furthermore, resistance measurements were carried out in the function of temperature to define the energy activation of the manufactured electrode. Samples were measured with a two-probe method in the temperature range of −180 to 60 °C with a 15 °C step. Obtained Arrhenius plot shown in Fig. 4 allowed us to estimate activation energy $E_a = 115.2$ meV, which is higher than the usual BDD electrode [80,81], and almost three times higher than unmodified RVC foam ($E_a = 29.3$ meV). This fact exhibits the complex structure of the semiconducting BDNC@RVC electrode composed of BDD, DCNW and of the planar graphenic layer revealing a variable distance hopping charge transfer mechanism [82]. Experimental data of unmodified RVC coincide with the data provided by the manufacturer [83].

Table 2
Calculation of porosity for bare RVC and BDNC@RVC anodes.

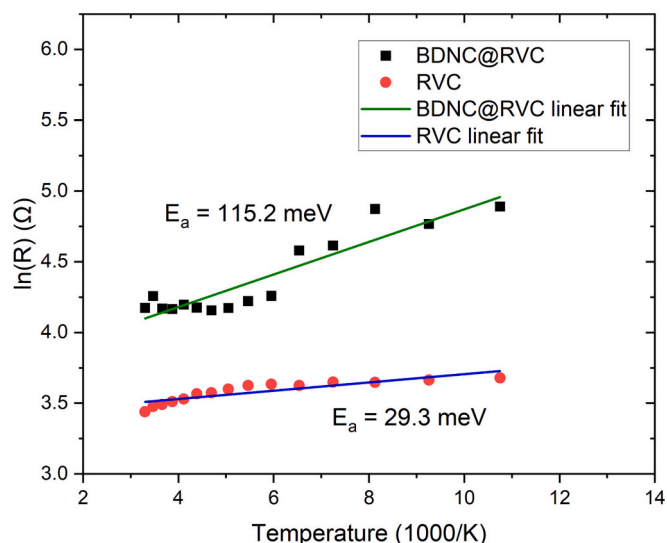| Sample	ROI volume/ (mm³)	Solid material volume in ROI (mm³)	Pores volume in ROI (mm³)	Volume porosity (%)	Solid material surface in ROI (mm²)	Pore surface in ROI (mm²)	Surface porosity (%)
Bare RVC	828.60	56.45	772.15	93.19	987.55	2001.33	66.96
BDD@RVC	737.69	47.40	690.29	93.57	836.02	1758.29	68.77

Fig. 4. Arrhenius plot of BDNC@RVC anode (black squares) and unmodified RVC (red dots) in a temperature range of −180 to 60 °C.

3.2. Studies of redox kinetics at RVC and BDNC@RVC electrodes

The CV comparative analysis of the $Fe(CN)_6^{3-/4-}$ redox probe kinetics is presented in Fig. 5. As the general observation, BDNC@RVC electrodes are characterized with higher peak current densities than non-modified porous carbon structure, which indicates that the layer of nanomaterials including GR, BDD/CNW, BDD layers possesses an appropriate structure and electronic properties enabling effective electron transfer through the electrode/electrolyte interphase.

While the $Fe(CN)_6^{3-/4-}$ redox process should be considered irreversible for both studied electrode materials (peak-to-peak separation $\Delta Ep > 59$ mV in CV scan [67]), the situation significantly improved upon surface modification. The detailed ΔEp values for each studied scan are summarized in Table 3. For example, at $\nu = 50$ mV s^{-1} the BDNC@RVC electrode is characterized with $\Delta Ep = 194.9$ mV, compared to 292.6 mV for unmodified RVC. The symmetric anodic-to-cathodic current density ratio $j_a/j_c \approx 1$ gives further testimony of the improved process reversibility. Moreover, the enhanced electrode kinetics of the BDNC@RVC electrode manifests itself by nearly twice as high CV peak current densities (0.58 mA cm^{-2} compared to 0.37 for bare RVC). Following that the process should still be considered irreversible, a good linear dependence of the $I_p = f(\nu^{1/2})$ was achieved, see Fig. 5D. A lower value of the linear coefficient for RVC suggests sluggish, activation-controlled, heterogeneous electron transfer processes.

Following a linear relationship of the $I_p = f(\nu^{1/2})$ function, the electrochemically active surface area (EASA), was estimated for each sample and compared with the geometric surface area A. The observed EASA:A ratio was significantly different and as little as 61 % for RVC, compared to a terrific 132 % for BDNC@RVC (see Table S2). The obtained results suggest an increase in the electrochemically active surface area by nearly 114 % after BDNC deposition and contribute an important observation. In contrast to BDD@RVC electrode, unmodified RVC electrode characterized a sluggish electron transfer mechanism. After chemical vapor deposition treatment RVC surface is characterized by multiple crystallites, defects, and nondiamond amorphous carbon impurity phases would provide sites for heterogeneous electron transfer. The BDNC@RVC electrode shows the characteristic of an overlapping diffusion layer of active species, indicates a higher faradaic current and efficient electron transfer process. In case of the unmodified RVC
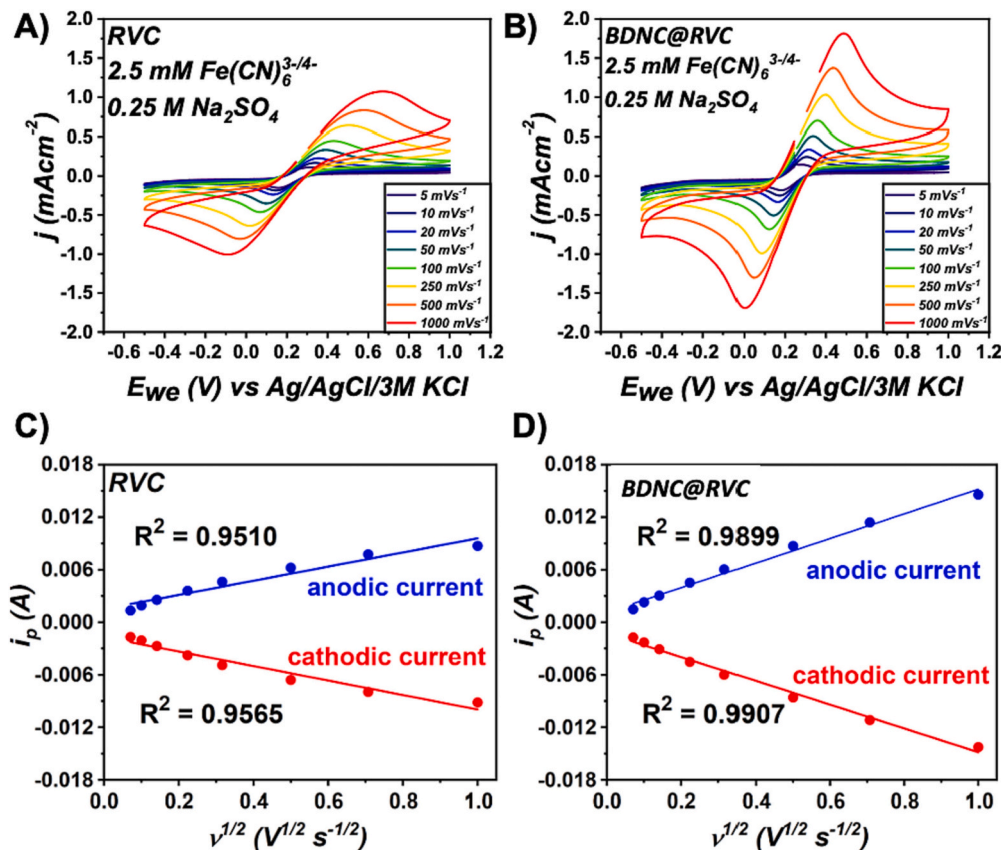

Fig. 5. Cyclic voltammograms of the electron transfer for 2.5 mM $[Fe(CN)_6]^{3-/4-}$ in 0.25 M Na$_2$SO$_4$ solution on the A) bare RVC and B) BDNC@RVC anodes; C, D) depicts the corresponding ip = f(ν1/2) graphs. CV scan rate: 5–1000 mV s^{-1}.

Table 3
The characteristics of the $Fe(CN)_6^{3-/4-}$ redox process for RVC and BDNC@RVC electrodes, based on CV scans.

| Scan rate	$E_{p,A}$	$J_{p,A}$	$E_{p,C}$	$J_{p,C}$	ΔE_p	$J_{p,A}/J_{p,C}$
mV s^{-1}	V	mA cm^{-2}	V	mA cm^{-2}	mV	–
RVC						
5	0.312	0.140	0.158	0.175	154.2	0.80
10	0.338	0.200	0.147	0.215	190.7	0.93
20	0.355	0.266	0.132	0.284	223.2	0.94
50	0.392	0.374	0.099	0.394	292.6	0.95
100	0.429	0.482	0.068	0.511	360.7	0.94
250	0.505	0.648	0.017	0.687	487.5	0.94
500	0.579	0.808	−0.030	0.830	608.9	0.97
1000	0.632	0.909	−0.067	0.955	699.1	0.95
BDNC@RVC						
5	0.283	0.189	0.182	0.223	100.6	0.85
10	0.306	0.294	0.173	0.294	133.0	1.00
20	0.316	0.390	0.164	0.395	152.4	0.99
50	0.337	0.579	0.142	0.580	194.9	1.00
100	0.359	0.773	0.122	0.770	237.0	1.00
250	0.397	1.118	0.087	1.102	309.8	1.01
500	0.436	1.461	0.049	1432	387.2	1.02
1000	0.488	1.868	0.003	1.828	485.3	1.02

surface, the scale of the insulating species may be extremely high that the electroactive species show individual linear diffusion layers [84]. The non-homogeneous charge transfer through various RVC segments directly affects the electrode performance. On the other hand, the number of active sites developed through layer of nanomaterials including GR, BDD/CNW, BDD deposits rises pronouncedly, translating to higher redox currents but also more spatially homogeneous electron transfer and thus, process reversibility. It should be noted that the ferrocyanides electron transfer mechanism is known to be the inner sphere reaction. In the result, reaction kinetic translates into the chemical compositions of the investigated surfaces, because the capability of effective electron transfer requires direct interactions with reactive sites on the electrode. However, it is not sensitive to oxide bonding on the electrode surface [85]. Utilizing this redox probe allows for effective differentiation of process kinetics that originates from different functionalization groups at the electrode surface.

It may be concluded that the presence of boron-doped diamondized nanocarbon films on the RVC foam at sufficiently high boron doping

density leads to more effective redox kinetics and higher values of the standard heterogeneous rate constant $k^0 = 8.24 \cdot 10^{-4}$ cm s^{-1}, estimated using the Nicholson approach [66]. For bare RVC surface, the value k^0 is twice smaller ($k^0 = 4.14 \cdot 10^{-4}$ cm s^{-1}). The incorporation of boron atoms into the NC lattice, predominantly determined through Raman spectral analysis, plays an important role in the nucleation and growth of nanocarbons and subsequently in the observed enhancement of charge transfer kinetics at BDNC@RVC electrodes [86]. Furthermore, the formation of sp^2 hybridized carbon phases, supplied with edge dislocations and an expanded surface area, represents another significant factor that apparently contributes to the improved electrochemical performance [87,88]. The high EASA and superior heterogeneous rate constant k^0 of BDNC@RVC makes the electrode more attractive for potential electrocatalysis applications. The electrochemical impedance spectroscopy studies support previous conclusions. The EIS Nyquist plots are depicted in Fig. 6.

The plots registered for both studied samples displayed semicircle patterns covering the high-frequency region, with a 45° slope line in the low-frequency region that reflects the charge transfer process at the electrode/electrolyte interface and mass diffusion control, respectively [89]. Quantitative data were estimated using an electric equivalent circuit (EEQC) in the EC-Lab software. The EEQC used for fitting was $R_E(CPE(R_{CT}W))$ [90] with normalized fitting error $\chi^2 \approx 10^{-4}$. In the proposed circuit, R_E refers to the series resistance, made up of three components: the resistance caused by the ions in the electrolyte, the resistance inherent in the active material itself, and the resistance at the interface between the electroactive material and the current collector. Constant phase element (CPE) was proposed to represent the non-ideal behavior of the electric double layer capacitance due to spatial heterogeneities at the electrode/electrolyte interphase and porosity. The CPE is represented by an impedance expression of the form: $Z_{CPE} = [Q(j\omega)]^{-\alpha}$, where Q is the quasi-capacitance, ω is the angular frequency, and α is the CPE exponent. When $\alpha = 1$, the CPE represents an ideal capacitor, thus its deviation from this value represents the heterogeneity factor [91,92]. Next, R_{CT} represents resistance associated with the redox process. W is
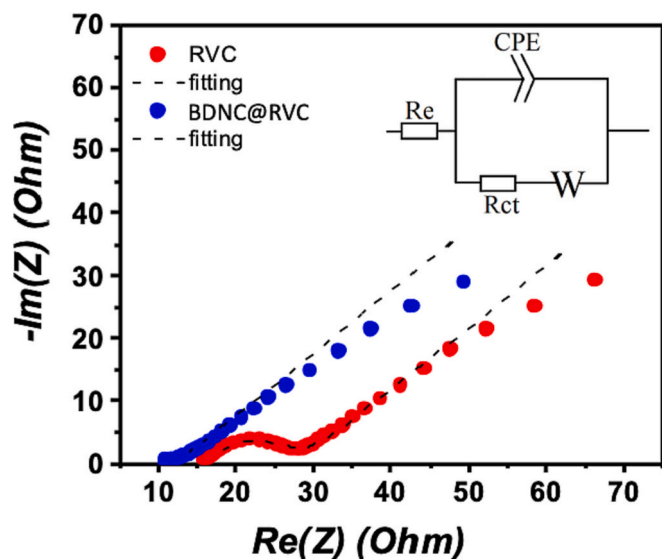
Fig. 6. EIS spectra of RVC and BDNC@RVC anodes measured at OCP in 2.5 mM $[Fe(CN)_6]^{3-/4-}$ + 0.25 M Na$_2$SO$_4$. Frequency range: $1 \cdot 10^5$ to $1 \cdot 10^{-2}$ Hz.

Table 4
EIS analysis results using $R_E(CPE(R_{CT}W))$ EEQC.

Sample	Re/Ω cm^{-2}	R$_{ct}$/Ω cm^{-2}	CPE/Ss$^\alpha$ cm^2	α
RVC	116.3	91.37	0.222	0.81
BDNC@RVC	73.0	7.95	1.537	0.86

Warburg impedance, describing the diffusion of species through a semi-infinite layer [93].

Concluding the EEQC fitting results, given in Table 4, the EIS confirms a significant, one order-of-magnitude RCT drop upon surface modification with BDD and other boron-doped nanocarbon derivatives. Furthermore, the CPE exponent α increases from 0.81 to 0.86 indicating a decrease in the frequency dispersion of capacitance and a rise in electrode homogeneity.

The charge transfer resistance is closely related to the reaction exchange current and rate of electrochemical reaction [94]. Decreasing of charge transfer resistance (RCT) is expected to translate directly into more efficient degradation of APAP, as it involves a higher rate of electrode reactions, oxidation of active species and generation of radicals [95–99].

3.3. APAP electrooxidation on RVC and BDNC@RVC electrodes

Fabrication of BDNC@RVC structures strongly impacts the overall electrode kinetics, affecting the electrochemical stability window of the electrolyte as well as the degradation pathway for organic pollutants' electrooxidation [100]. RVC and BDNC are two different types of anode materials, that are associated with altered adsorption energies, activation overpotentials, and so on. RVC surface, likewise glassy carbon (GC), eagerly interacts with hydroxyl radicals and transforms into a higher oxide or superoxide [101–103]. BDD is a non-active anode, the surface does not provide any catalytic site for the adsorption of organic compounds from the aqueous medium, and it performs a sink electron function for the removal of electrons [104]. Moreover, as we reported before, the BDNC modification is, in fact, a superposition of various boron-enriched carbon nanoarchitectures [65,70,105].

Both GC and BDNC are characterized by wide electrochemical windows [106], this feature does not seem to be largely affected when studied in an aqueous 0.1 M Na_2SO_4 solution, as observed in Fig. 7. Introducing 200 mg L^{-1} APAP reveals that an oxidation peak is shifted from E = 1.175 V (for bare RVC) down to 0.963 V vs Ag/AgCl/3 M KCl

resulting in 212 mV difference, when the oxidation is carried out at BDNC@RVC. This effect should be ascribed to lower activation overpotential because of the reduced energy barrier required to initiate the reaction. Moreover, higher APAP oxidation currents observed (1.44 mA cm^{-2} for BDNC@RVC vs 0.94 mA cm^{-2} for bare RVC) indicate enhanced kinetics, plausibly due to higher EASA and a higher number of active sites at the electrode surface. The energy input to drive the APAP decomposition reactions at BDNC@RVC is also lower, which is crucial for sustainable and cost-effective water treatment.

The APAP decomposition route was followed using UHPLC-HRAM-MS. The results allowed to identify some aromatic compounds, the products of APAP direct oxidation at RVC and BDNC@RVC electrodes [107,108], the proposed oxidation mechanism is in Fig. S2 [27,109].

The direct anodic oxidation of APAP reactions resulted in the formation of two intermediate compounds: hydroquinone and 4-aminophenol which was oxidized to 4-nitrophenol [28]. It's worth highlighting that benzoquinone, typically expected in such degradation processes, was conspicuously absent in the range of intermediates and end products generated [28,]. Further, oxidation of these intermediates leads to the generation of carboxylic acids, namely muconic acid, oxamic acid, and malonic acid [115,116]. Additionally, the BDNC@RVC electrode yielded lower amounts of carboxylic acids. These observations suggest APAP oxidation process via a direct electron transfer process occurs more effectively at the BDNC@RVC electrode surface than at the bare RVC electrode.

Overall, our findings reveal that BDNC@RVC is substantially more effective when it comes to APAP decomposition. The galvanostatic electrolysis at 0.7 mA cm^{-2} during 4 h attained APAP degradation rates of 66 and 78 % for RVC and BDNC@RVC, respectively, which is an explicit effect of high EASA development with numerous active sites and decisive charge transfer kinetics. This effect might be also attributed to porous 3D structures inducing disturbance to fluid flow [120].

4. Conclusions

We have used Microwave Plasma Chemical Vapor Deposition (MWCVD) to deposit boron-doped diamondized nanocarbons onto three-dimensional reticulated vitreous carbon (RVC) structures results in multi structural film depending on distance from plasma source. Raman spectroscopy and SEM topography studies of the BDNC@RVC electrode revealed different layers on the RVC foam depending on the distance from the plasma, resulting in boron-rich nanocarbon structures. The content of sp^2-bonded carbon in the covered RVC foam by boron doped nanocarbon layers was found to increase with increasing distance from the plasma source. Notably the resultant electrode performance is an inseparable superposition of electron transfer through the multilayered system.

We have shown that boron-doped diamondized nanocarbons deposition significantly improves the electrochemical performance of the RVC structures, the effect to be combined with joint enhancement of the electrochemically-active surface area (by approx. 59 %) and the increase in heterogeneous rate constant k^0 from $4.14 \cdot 10^{-4}$ to $8.24 \cdot 10^{-4}$ cm s^{-1} after surface modification. These parameters were studied by CV using $Fe(CN)_6^{3-/4-}$ redox probe. The electron transfer through the bare RVC is less reversible and more sluggish, a characteristic of electrochemically heterogeneous surfaces. The R_{CT} value defined by EIS dropped by an order of magnitude to reach 7.95 Ω cm^{-2} for BDNC@RVC. Obtained results shows that deposition of boron-doped diamondized nanocarbons enhance the electroactivity of RVC foam towards APAP electrooxidation. The above-described features gave a prominent edge when using BDNC@RVC for the APAP electrooxidation process. The CV studies reveal a decrease in activation overpotentials of APAP oxidation by 212 mV, implying lower energy requirements to transfer an electron through the interface. The results showed 12 % higher APAP decomposition efficiency compared to bare RVC, yielding lower amounts of intermediates such as carboxylic acids. Energy activation (E_a) analysis,
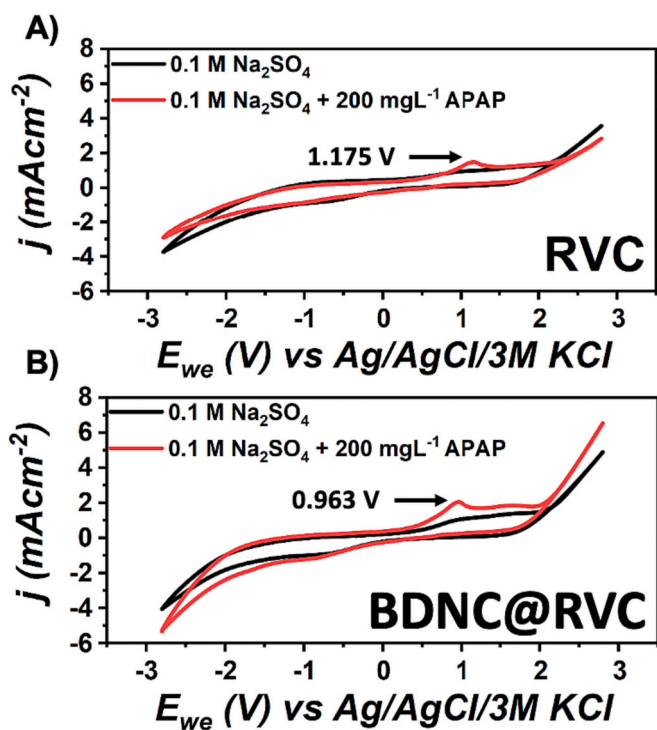

Fig. 7. Cyclic voltammogram of A) RVC and B) BDNC@RVC anodes in 0.1 M Na_2SO_4 as electrolyte and 0.1 M Na_2SO containing 200 mg L^{-1} APAP. Scan rate 100 mV s^{-1}.

which provides insight into the energy required to initiate a chemical reaction, indicated a value of only 115.2 meV for BDNC@RVC, supporting the previous finding of lower energy demand.

Nonetheless, despite the concern pointed out by the Reviewer regarding not meeting the final goal and not being able to uniformly grow homogeneous BDD film through different depths of the RVC architecture, we have managed to obtain a much better understanding of the 3D-structure related CVD growth chemistry, which is being shared in this manuscript. Furthermore, our results clearly demonstrate a significant enhancement of the redox process kinetics offered by the BDNC electrode.

Author statement

I write on behalf of myself and all co-authors to confirm that the results reported in the manuscript are original and neither the entire work, nor any of its parts have been previously published. The authors confirm that the article has not been submitted to peer-review, nor has been accepted for publishing in another journal. The authors confirm that the research in their work is original, and that all the data given in the article are real and authentic. If necessary, the article can be recalled, and errors corrected.

CRediT authorship contribution statement

Iwona Kaczmarzyk: Data curation, Formal analysis, Investigation, Methodology, Writing – original draft. **Mariusz Banasiak:** Formal analysis, Investigation, Writing – original draft. **Paweł Jakóbczyk:** Data curation, Formal analysis, Investigation, Methodology, Writing – original draft. **Michał Sobaszek:** Conceptualization, Investigation, Writing – original draft, Writing – review & editing. **Gabriel Strugała:** Investigation, Writing – original draft. **Tomasz Seramak:** Investigation, Writing – original draft. **Paweł Rostkowski:** Investigation. **Jakub Karczewski:** Investigation. **Mirosław Sawczak:** Formal analysis, Investigation, Writing – original draft. **Jacek Ryl:** Supervision, Validation, Writing – original draft, Writing – review & editing. **Robert Bogdanowicz:** Conceptualization, Supervision, Validation, Funding acquisition, Project administration, Writing – review & editing.

Declaration of competing interest

The authors declare the following financial interests/personal relationships which may be considered as potential competing interests:
Robert Bogdanowicz reports financial support was provided by National Centre for Research and Development.

Data availability

No data was used for the research described in the article.

Acknowledgements

Appendix A. Supplementary data

Supplementary data to this article can be found online at https://doi.org/10.1016/j.diamond.2023.110673.

References

[1] M. Bohner, Design of ceramic-based cements and putties for bone graft substitution, Eur. Cell. Mater. 20 (2010) 1–12, https://doi.org/10.22203/ecm.v020a01.

[2] J.M. Friedrich, C. Ponce-de-León, G.W. Reade, F.C. Walsh, Reticulated vitreous carbon as an electrode material, J. Electroanal. Chem. 561 (2004) 203–217, https://doi.org/10.1016/j.jelechem.2003.07.019.

[3] J. Wang, N. Naser, Reticulated vitreous carbon-plant tissue composite bioelectrodes, Anal. Chim. Acta 242 (1991) 259–265, https://doi.org/10.1016/0003-2670(91)87073-G.

[4] S.Z.J. Zaidi, C. Harito, F.C. Walsh, C. Ponce de León, Decolourisation of reactive black-5 at an RVC substrate decorated with PbO2/TiO2 nanosheets prepared by anodic electrodeposition, J. Solid State Electrochem. 22 (2018) 2889–2900, https://doi.org/10.1007/s10008-018-3992-1.

[5] L. de S. Vieira, A review on the use of glassy carbon in advanced technological applications, Carbon 186 (2022) 282–302, https://doi.org/10.1016/j.carbon.2021.10.022.

[6] C. Dalmolin, S.R. Biaggio, R.C. Rocha-Filho, N. Bocchi, Reticulated vitreous carbon/polypyrrole composites as electrodes for lithium batteries: preparation, electrochemical characterization and charge–discharge performance, Synth. Met. 160 (2010) 173–179, https://doi.org/10.1016/j.synthmet.2009.10.028.

[7] E.J. Fraser, J.P. Le Houx, L.F. Arenas, K.K.J.R. Dinesh, R.G.A. Wills, The soluble lead flow battery: image-based modelling of porous carbon electrodes, J. Energy Storage 52 (2022), 104791, https://doi.org/10.1016/j.est.2022.104791.

[8] G. Lepage, F.O. Albernaz, G. Perrier, G. Merlin, Characterization of a microbial fuel cell with reticulated carbon foam electrodes, Bioresour. Technol. 124 (2012) 199–207, https://doi.org/10.1016/j.biortech.2012.07.067.

[9] K. Fei, T. Song, H. Wang, D. Zhang, R. Tao, J. Xie, Electrophoretic deposition of carbon nanotube on reticulated vitreous carbon for hexavalent chromium removal in a biocathode microbial fuel cell, R. Soc. Open Sci. 4 (2017), 170798, https://doi.org/10.1098/rsos.170798.

[10] W.R. Strong, A.R. Knauff, B.W. Fravel, M.J. Samide, Introduction of ion-exchange moieties to reticulated vitreous carbon by direct chemical modification, Carbon 44 (2006) 1936–1941, https://doi.org/10.1016/j.carbon.2006.02.022.

[11] J. Tramontina, G. Machado, D.S. Azambuja, C.M.S. Piatnicki, D. Samios, Removal of Cd+2 from aqueous solutions onto polypyrrole coated reticulated vitreous carbon eletrodes, Mater. Res. 4 (2001) 195–200, https://doi.org/10.1590/S1516-14392001000300009.

[12] V.M. Vasconcelos, G.O.S. Santos, K.I.B. Eguiluz, G.R. Salazar-Banda, I. de Fatima Gimenez, Recent advances on modified reticulated vitreous carbon for water and wastewater treatment – a mini-review, Chemosphere 286 (2022) 131573, https://doi.org/10.1016/j.chemosphere.2021.131573.

[13] Y. Jin, Y. Shi, R. Chen, X. Chen, X. Zheng, Y. Liu, Electrochemical disinfection using a modified reticulated vitreous carbon cathode for drinking water treatment, Chemosphere 215 (2019) 380–387, https://doi.org/10.1016/j.chemosphere.2018.10.057.

[14] K.N. Knust, M.P. Foley, M.S. Mubarak, S. Skljarevski, K. Raghavachari, D.G. Peters, Electrochemical reduction of 5-chloro-2-(2,4-dichlorophenoxy)phenol (triclosan) in dimethylformamide, J. Electroanal. Chem. 638 (2010) 100–108, https://doi.org/10.1016/j.jelechem.2009.10.012.

[15] R.H. Tammam, A.H. Touny, M.M. Saleh, Removal of urea from dilute streams using RVC/nano-NiOx-modified electrode, Environ. Sci. Pollut. Res. 25 (2018) 19898–19907, https://doi.org/10.1007/s11356-018-2223-8.

[16] G. Ramírez, F.J. Recio, P. Herrasti, C. Ponce-de-León, I. Sirés, Effect of RVC porosity on the performance of PbO2 composite coatings with titanate nanotubes for the electrochemical oxidation of azo dyes, Electrochim. Acta 204 (2016) 9–17, https://doi.org/10.1016/j.electacta.2016.04.054.

[17] F.L. Rivera, N. Menendez, E. Mazarío, P. Herrasti, Electrofenton with reticular vitreous carbon and Iron oxide nanoparticles for dye removal: a preliminary study, Appl. Sci. 12 (2022) 8293, https://doi.org/10.3390/app12168293.

[18] A. Alverez-Gallegos, D. Pletcher, The removal of low level organics via hydrogen peroxide formed in a reticulated vitreous carbon cathode cell. Part 2: the removal of phenols and related compounds from aqueous effluents, Electrochim. Acta 44 (1999) 2483–2492, https://doi.org/10.1016/S0013-4686(98)00371-5.

[20] F.C. Walsh, L.F. Arenas, C. Ponce de León, G.W. Reade, I. Whyte, B.G. Mellor, The continued development of reticulated vitreous carbon as a versatile electrode material: structure, properties and applications, Electrochim. Acta 215 (2016) 566–591, https://doi.org/10.1016/j.electacta.2016.08.103.

[21] S. Wang, X. Zhang, E. Marsili, Electrochemical characteristics of Shewanella loihica PV-4 on reticulated vitreous carbon (RVC) with different potentials applied, Molecules 27 (2022) 5330, https://doi.org/10.3390/molecules27165330.

[22] A. Aldalbahi, M. Rahaman, M. Almoiqli, A strategy to enhance the electrode performance of novel three-dimensional PEDOT/RVC composites by electrochemical deposition method, Polymers 9 (2017) 157, https://doi.org/10.3390/polym9050157.

[23] V. Flexer, J. Chen, B.C. Donose, P. Sherrell, G.G. Wallace, J. Keller, The nanostructure of three-dimensional scaffolds enhances the current density of microbial bioelectrochemical systems, Energ. Environ. Sci. 6 (2013) 1291, https://doi.org/10.1039/c3ee00052d.

[24] A. Aldalbahi, M. Rahaman, M. Almoigli, A. Meriey, K. Alharbi, Improvement in electrode performance of novel SWCNT loaded three-dimensional porous RVC composite electrodes by electrochemical deposition method, Nanomaterials 8 (2018) 19, https://doi.org/10.3390/nano8010019.

[25] A. Aldalbahi, M. Rahaman, M. Almoiqli, A. Hamedelniel, A. Alrehaili, Single-walled carbon nanotube (SWCNT) loaded porous reticulated vitreous carbon (RVC) electrodes used in a capacitive deionization (CDI) cell for effective desalination, Nanomaterials 8 (2018) 527, https://doi.org/10.3390/nano8070527.

[26] A. Aldalbahi, M. Rahaman, M. Almoiqli, Performance enhancement of modified 3D SWCNT/RVC electrodes using microwave-irradiated graphene oxide, Nanoscale Res. Lett. 14 (2019) 351, https://doi.org/10.1186/s11671-019-3174-9.

[27] H.C. Arredondo Valdez, G. García Jiménez, S. Gutiérrez Granados, C. Ponce de León, Degradation of paracetamol by advance oxidation processes using modified reticulated vitreous carbon electrodes with TiO2 and CuO/TiO2/Al2O3, Chemosphere 89 (2012) 1195–1201, https://doi.org/10.1016/j.chemosphere.2012.07.020.

[28] E. Brillas, I. Sirés, C. Arias, P.L. Cabot, F. Centellas, R.M. Rodríguez, J.A. Garrido, Mineralization of paracetamol in aqueous medium by anodic oxidation with a boron-doped diamond electrode, Chemosphere 58 (2005) 399–406, https://doi.org/10.1016/j.chemosphere.2004.09.028.

[29] J. Millán-Barba, H. Bakkali, F. Lloret, M. Gutiérrez, R. Guzmán de Villoria, M. Domínguez, K. Haenen, D. Araujo, Boron-doped diamond growth on carbon fibre: enhancing the electrical conductivity, Appl. Surf. Sci. 615 (2023), 156382, https://doi.org/10.1016/j.apsusc.2023.156382.

[30] A.V. Diniz, V.J. Trava-Airoldi, E.J. Corat, N.G. Ferreira, Micro and nanocrystalline diamond formation on reticulated vitreous carbon substrate, Chem. Phys. Lett. 414 (2005) 412–416, https://doi.org/10.1016/j.cplett.2005.08.100.

[31] M.R. Baldan, S.C. Ramos, E.C. Almeida, A.F. Azevedo, N.G. Ferreira, Homogeneous micro and nanocrystalline diamond coating on reticulated vitreous carbon treated at different temperatures, Diamond Relat. Mater. 17 (2008) 1110–1115, https://doi.org/10.1016/j.diamond.2008.01.096.

[32] A. Fabiańska, T. Ossowski, R. Bogdanowicz, J. Czupryniak, M. Gnyba, T. Odzga, S.D. Janssens, K. Haenen, E.M. Siedlecka, Electrochemical oxidation of ionic liquids at highly boron doped diamond electrodes: electrochemical oxidation of ionic liquids, Phys. Status Solidi A 209 (2012) 1797–1803, https://doi.org/10.1002/pssa.201200056.

[33] J. Barjon, N. Habka, C. Mer, F. Jomard, J. Chevallier, P. Bergonzo, Resistivity of boron doped diamond: resistivity of boron doped diamond, Phys. Stat. Sol. (RRL) 3 (2009) 202–204, https://doi.org/10.1002/pssr.200903097.

[34] O.M. Cornejo, M.F. Murrieta, L.F. Castañeda, J.L. Nava, Characterization of the reaction environment in flow reactors fitted with BDD electrodes for use in electrochemical advanced oxidation processes: a critical review, Electrochim. Acta 331 (2020) 135373, https://doi.org/10.1016/j.electacta.2019.135373.

[35] S. Baluchová, A. Daňhel, H. Dejmková, V. Ostatná, M. Fojta, K. Schwarzová-Pecková, Recent progress in the applications of boron doped diamond electrodes in electroanalysis of organic compounds and biomolecules – a review, Anal. Chim. Acta 1077 (2019) 30–66, https://doi.org/10.1016/j.aca.2019.05.041.

[36] S. Sabatino, A. Galia, O. Scialdone, Electrochemical abatement of organic pollutants in continuous-reaction systems through the assembly of microfluidic cells in series, ChemElectroChem 3 (2016) 83–90, https://doi.org/10.1002/celc.201500409.

[37] A.M. Polcaro, A. Vacca, M. Mascia, S. Palmas, Oxidation at boron doped diamond electrodes: an effective method to mineralise triazines, Electrochim. Acta 50 (2005) 1841–1847, https://doi.org/10.1016/j.electacta.2004.08.037.

[38] M. Pierpaoli, M. Szopińska, B.K. Wilk, M. Sobaszek, A. Łuczkiewicz, R. Bogdanowicz, S. Fudala-Książek, Electrochemical oxidation of PFOA and PFOS in landfill leachates at low and highly boron-doped diamond electrodes, J. Hazard. Mater. 403 (2021), 123606, https://doi.org/10.1016/j.jhazmat.2020.123606.

[39] J. Iniesta, Electrochemical oxidation of phenol at boron-doped diamond electrode, Electrochim. Acta 46 (2001) 3573–3578, https://doi.org/10.1016/S0013-4686(01)00630-2.

[40] R. Bogdanowicz, A. Fabiańska, L. Golunski, M. Sobaszek, M. Gnyba, J. Ryl, K. Darowicki, T. Ossowski, S.D. Janssens, K. Haenen, E.M. Siedlecka, Influence of the boron doping level on the electrochemical oxidation of the azo dyes at Si/BDD thin film electrodes, Diamond Relat. Mater. 39 (2013) 82–88, https://doi.org/10.1016/j.diamond.2013.08.004.

[41] E. Brillas, C.A. Martínez-Huitle, Decontamination of wastewaters containing synthetic organic dyes by electrochemical methods. An updated review, Appl. Catal. B Environ. 166–167 (2015) 603–643, https://doi.org/10.1016/j.apcatb.2014.11.016.

[42] B. Marselli, J. Garcia-Gomez, P.-A. Michaud, M.A. Rodrigo, C. Comninellis, Electrogeneration of hydroxyl radicals on boron-doped diamond electrodes, J. Electrochem. Soc. 150 (2003) D79, https://doi.org/10.1149/1.1553790.

[43] L. Bu, S. Zhu, S. Zhou, Degradation of atrazine by electrochemically activated persulfate using BDD anode: role of radicals and influencing factors, Chemosphere 195 (2018) 236–244, https://doi.org/10.1016/j.chemosphere.2017.12.088.

[44] H. Song, L. Yan, J. Jiang, J. Ma, Z. Zhang, J. Zhang, P. Liu, T. Yang, Electrochemical activation of persulfates at BDD anode: radical or nonradical oxidation? Water Res. 128 (2018) 393–401, https://doi.org/10.1016/j.watres.2017.10.018.

[45] S.H. Din, M.A. Shah, N.A. Sheikh, M.M. Butt, CVD diamond, Trans. Indian Inst. Metals 72 (2019) 1–9, https://doi.org/10.1007/s12666-018-1454-1.

[46] R.J. Nemanich, J.A. Carlisle, A. Hirata, K. Haenen, CVD diamond—research, applications, and challenges, MRS Bull. 39 (2014) 490–494, https://doi.org/10.1557/mrs.2014.97.

[47] D. Damm, A. Contin, F. Barbieri, V. Trava-Airoldi, D. Barquete, E. Corat, Interlayers applied to CVD diamond deposition on steel substrate: a review, Coatings 7 (2017) 141, https://doi.org/10.3390/coatings7090141.

[48] A. Tallaire, V. Mille, O. Brinza, T.N. Tran Thi, J.M. Brom, Y. Loguinov, A. Katrusha, A. Koliadin, J. Achard, Thick CVD diamond films grown on high-quality type IIa HPHT diamond substrates from new diamond technology,

[49] A. Tallaire, J. Achard, A. Boussadi, O. Brinza, A. Gicquel, I.N. Kupriyanov, Y. N. Palyanov, G. Sakr, J. Barjon, High quality thick CVD diamond films homoepitaxially grown on (111)-oriented substrates, Diamond Relat. Mater. 41 (2014) 34–40, https://doi.org/10.1016/j.diamond.2013.11.002.

[50] S. Garcia-Segura, E. Vieira dos Santos, C.A. Martínez-Huitle, Role of sp3/sp2 ratio on the electrocatalytic properties of boron-doped diamond electrodes: a mini review, Electrochem. Commun. 59 (2015) 52–55, https://doi.org/10.1016/j.elecom.2015.07.002.

[51] N.R. Wilson, S.L. Clewes, M.E. Newton, P.R. Unwin, J.V. Macpherson, Impact of grain-dependent boron uptake on the electrochemical and electrical properties of polycrystalline boron doped diamond electrodes, J. Phys. Chem. B 110 (2006) 5639–5646, https://doi.org/10.1021/jp0547616.

[52] K. Ushizawa, K. Watanabe, T. Ando, I. Sakaguchi, M. Nishitani-Gamo, Y. Sato, H. Kanda, Boron concentration dependence of Raman spectra on {100} and {111} facets of B-doped CVD diamond, Diamond Relat. Mater. 7 (1998) 1719–1722, https://doi.org/10.1016/S0925-9635(98)00296-9.

[53] M.C. Granger, M. Witek, J. Xu, J. Wang, M. Hupert, A. Hanks, M.D. Koppang, J. E. Butler, G. Lucazeau, M. Mermoux, J.W. Strojek, G.M. Swain, Standard electrochemical behavior of high-quality, boron-doped polycrystalline diamond thin-film electrodes, Anal. Chem. 72 (2000) 3793–3804, https://doi.org/10.1021/ac0000675.

[54] J. Ryl, L. Burczyk, R. Bogdanowicz, M. Sobaszek, K. Darowicki, Study on surface termination of boron-doped diamond electrodes under anodic polarization in H2SO4 by means of dynamic impedance technique, Carbon 96 (2016) 1093–1105, https://doi.org/10.1016/j.carbon.2015.10.064.

[55] X.-R. Lu, M.-H. Ding, C. Zhang, W.-Z. Tang, Comparative study on stability of boron doped diamond coated titanium and niobium electrodes, Diamond Relat. Mater. 93 (2019) 26–33, https://doi.org/10.1016/j.diamond.2019.01.010.

[56] A. Zielinski, M. Cieslik, M. Sobaszek, R. Bogdanowicz, J. Ryl, Multifrequency nanoscale impedance microscopy (m-NIM): a novel approach towards detection of selective and subtle modifications on the surface of polycrystalline boron-doped diamond electrodes, Ultramicroscopy 199 (2019) 34–45, https://doi.org/10.1016/j.ultramic.2019.01.004.

[57] T. Kashiwada, T. Watanabe, Y. Ootani, Y. Tateyama, Y. Einaga, A study on electrolytic corrosion of boron-doped diamond electrodes when decomposing organic compounds, ACS Appl. Mater. Interfaces 8 (2016) 28299–28305, https://doi.org/10.1021/acsami.5b11638.

[58] R. Trouillon, D. O'Hare, Comparison of glassy carbon and boron doped diamond electrodes: resistance to biofouling, Electrochim. Acta 55 (2010) 6586–6595, https://doi.org/10.1016/j.electacta.2010.06.016.

[59] E. Scorsone, N. Gattout, L. Rousseau, G. Lissorgues, Porous diamond pouch cell supercapacitors, Diamond Relat. Mater. 76 (2017) 31–37, https://doi.org/10.1016/j.diamond.2017.04.004.

[60] J. Zhang, X. Yu, Z. Zhang, J. Li, Z.-Y. Zhao, Adjusting pore size and shape to achieve the desired capacitance of boron-doped diamond electrodes, Surf. Rev. Lett. 26 (2019), 1830009, https://doi.org/10.1142/S0218625X18300095.

[61] X. Wang, Y. He, Z. Guo, Z. Huang, P. Zhang, H. Lin, Enhanced electrochemical supercapacitor performance with a three-dimensional porous boron-doped diamond film, New J. Chem. 43 (2019) 18813–18822, https://doi.org/10.1039/C9NJ04019F.

[62] Z. Vlčková Živcová, V. Mortet, A. Taylor, A. Zukal, O. Frank, L. Kavan, Electrochemical characterization of porous boron-doped diamond prepared using SiO2 fiber template, Diamond Relat. Mater. 87 (2018) 61–69, https://doi.org/10.1016/j.diamond.2018.05.007.

[63] L.G. Vernasqui, A.F. Sardinha, S.S. Oishi, N.G. Ferreira, Nanoscale control of high-quality boron-doped ultrananodiamond on dioxide titanium nanotubes as a porous composite, J. Mater. Res. Technol. 12 (2021) 597–612, https://doi.org/10.1016/j.jmrt.2021.02.099.

[64] I. Duo, A. Fujishima, C. Comninellis, Electron transfer kinetics on composite diamond (sp3)–graphite (sp2) electrodes, Electrochem. Commun. 5 (2003) 695–700, https://doi.org/10.1016/S1388-2481(03)00169-3.

[65] M. Pierpaoli, P. Jakobczyk, M. Sawczak, A. Łuczkiewicz, S. Fudala-Książek, R. Bogdanowicz, Carbon nanoarchitectures as high-performance electrodes for the electrochemical oxidation of landfill leachate, J. Hazard. Mater. 401 (2021), 123407, https://doi.org/10.1016/j.jhazmat.2020.123407.

[66] R.S. Nicholson, Theory and application of cyclic voltammetry for measurement of electrode reaction kinetics, Anal. Chem. 37 (1965) 1351–1355, https://doi.org/10.1021/ac60230a016.

[67] A.J. Bard, L.R. Faulkner, H.S. White, Electrochemical Methods: Fundamentals and Applications, Third edition, Wiley, Hoboken, NJ, 2022.

[68] R.M. Farinos, L.A.M. Ruotolo, Comparison of the electrooxidation performance of three-dimensional RVC/PbO2 and boron-doped electrodes, Electrochim. Acta 224 (2017) 32–39, https://doi.org/10.1016/j.electacta.2016.12.025.

[69] M. Marton, M. Vojs, M. Kotlár, P. Michniak, Ľ. Vančo, M. Veselý, R. Redhammer, Deposition of boron doped diamond and carbon nanomaterials on graphite foam electrodes, Appl. Surf. Sci. 312 (2014) 139–144, https://doi.org/10.1016/j.apsusc.2014.05.199.

[70] M. Sobaszek, K. Siuzdak, J. Ryl, M. Sawczak, S. Gupta, S.B. Carrizosa, M. Ficek, B. Dec, K. Darowicki, R. Bogdanowicz, Diamond phase (sp3-C) rich boron-doped carbon nanowalls (sp2-C): physicochemical and electrochemical properties, J. Phys. Chem. C 121 (2017) 20821–20833, https://doi.org/10.1021/acs.jpcc.7b06365.

[71] V. Mortet, A. Taylor, Z. Vlčková Živcová, D. Machon, O. Frank, P. Hubík, D. Tremouilles, L. Kavan, Analysis of heavily boron-doped diamond Raman

spectrum, Diamond Relat. Mater. 88 (2018) 163–166, https://doi.org/10.1016/j.diamond.2018.07.013.

[72] V. Mortet, Z. Vlčková Živcová, A. Taylor, O. Frank, P. Hubík, D. Trémouilles, F. Jomard, J. Barjon, L. Kavan, Insight into boron-doped diamond Raman spectra characteristic features, Carbon 115 (2017) 279–284, https://doi.org/10.1016/j.carbon.2017.01.022.

[73] I. Calizo, A.A. Balandin, W. Bao, F. Miao, C.N. Lau, Temperature dependence of the Raman spectra of graphene and graphene multilayers, Nano Lett. 7 (2007) 2645–2649, https://doi.org/10.1021/nl071033g.

[74] M.H. Joo, S.J. Park, S.-M. Hong, C.K. Rhee, D. Kim, G. Ji, S.W. Lee, Y. Sohn, X-ray micro computed tomography and efficient electrochemical recovery of lanthanides on porous carbon cylinder electrodes, Compos. Part B Eng. 231 (2022), 109590, https://doi.org/10.1016/j.compositesb.2021.109590.

[75] A. Szczurek, V. Fierro, A. Pizzi, M. Stauber, A. Celzard, Carbon meringues derived from flavonoid tannins, Carbon 65 (2013) 214–227, https://doi.org/10.1016/j.carbon.2013.08.017.

[76] M. Letellier, A. Szczurek, M.-C. Basso, A. Pizzi, V. Fierro, O. Ferry, A. Celzard, Preparation and structural characterisation of model cellular vitreous carbon foams, Carbon 112 (2017) 208–218, https://doi.org/10.1016/j.carbon.2016.11.017.

[77] L.F. Arenas, R.P. Boardman, C. Ponce de León, F.C. Walsh, X-ray computed micro-tomography of reticulated vitreous carbon, Carbon 135 (2018) 85–94, https://doi.org/10.1016/j.carbon.2018.03.088.

[78] K.-F. Cai, J.-P. Liu, C.-W. Nan, X.-M. Min, Effect of porosity on the thermal-electric properties of Al-doped SiC ceramics, J. Mater. Sci. Lett. 16 (1997) 1876–1878, https://doi.org/10.1023/A:1018557827330.

[79] J. Ihle, H.-P. Martin, M. Herrmann, P. Obenaus, J Adler, W. Hermel, A. Michaelis, The influence of porosity on the electrical properties of liquid-phase sintered silicon carbide, Int. J. Mater. Res. 97 (2006) 649–656, https://doi.org/10.3139/146.101285.

[80] M. Rycewicz, A. Nosek, D.H. Shin, M. Ficek, J.G. Buijnsters, R. Bogdanowicz, The effect of boron concentration on the electrical, morphological and optical properties of boron-doped nanocrystalline diamond sheets: tuning the diamond-on-graphene vertical junction, Diamond Relat. Mater. 128 (2022), 109225, https://doi.org/10.1016/j.diamond.2022.109225.

[81] M. Werner, R. Job, A. Zaitzev, W.R. Fahrner, W. Seifert, C. Johnston, P. R. Chalker, The relationship between resistivity and boron doping concentration of single and polycrystalline diamond, Phys. Stat. Sol. (A) 154 (1996) 385–393, https://doi.org/10.1002/pssa.2211540127.

[82] K.B. Holt, A.J. Bard, Y. Show, G.M. Swain, Scanning electrochemical microscopy and conductive probe atomic force microscopy studies of hydrogen-terminated boron-doped diamond electrodes with different doping levels, J. Phys. Chem. B 108 (2004) 15117–15127, https://doi.org/10.1021/jp048222x.

[83] R.F. Mamin, T. Inushima, Conductivity in boron-doped diamond, Phys. Rev. B 63 (2001), 033201, https://doi.org/10.1103/PhysRevB.63.033201.

[84] T.J. Davies, C.E. Banks, R.G. Compton, Voltammetry at spatially heterogeneous electrodes, J. Solid State Electrochem. 9 (2005) 797–808, https://doi.org/10.1007/s10008-005-0699-x.

[85] P. Chen, R.L. McCreery, Control of electron transfer kinetics at glassy carbon electrodes by specific surface modification, Anal. Chem. 68 (1996) 3958–3965, https://doi.org/10.1021/ac960492r.

[86] K. Siuzdak, M. Ficek, M. Sobaszek, J. Ryl, M. Gnyba, P. Niedziałkowski, N. Malinowska, J. Karczewski, R. Bogdanowicz, Boron-enhanced growth of micron-scale carbon-based nanowalls: a route toward high rates of electrochemical biosensing, ACS Appl. Mater. Interfaces 9 (2017) 12982–12992, https://doi.org/10.1021/acsami.6b16860.

[87] A.J. Pak, E. Paek, G.S. Hwang, Impact of graphene edges on enhancing the performance of electrochemical double layer capacitors, J. Phys. Chem. C 118 (2014) 21770–21777, https://doi.org/10.1021/jp504458z.

[88] J. Wu, M.-T.F. Rodrigues, R. Vajtai, P.M. Ajayan, Tuning the electrochemical reactivity of boron- and nitrogen-substituted graphene, Adv. Mater. 28 (2016) 6239–6246, https://doi.org/10.1002/adma.201506316.

[89] Electrochemistry., Principles, methods and applications, Electrochim. Acta 39 (1994) 853, https://doi.org/10.1016/0013-4686(94)80035-9.

[90] S.C.B. Oliveira, A.M. Oliveira-Brett, Voltammetric and electrochemical impedance spectroscopy characterization of a cathodic and anodic pre-treated boron doped diamond electrode, Electrochim. Acta 55 (2010) 4599–4605, https://doi.org/10.1016/j.electacta.2010.03.016.

[91] P. Niedzialkowski, P. Slepski, J. Wysocka, J. Chamier-Cieminska, L. Burczyk, M. Sobaszek, A. Wcislo, T. Ossowski, R. Bogdanowicz, J. Ryl, Multisine impedimetric probing of biocatalytic reactions for label-free detection of DEFB1 gene: how to verify that your dog is not human? Sens. Actuators B 323 (2020), 128664 https://doi.org/10.1016/j.snb.2020.128664.

[92] J. Ryl, L. Burczyk, A. Zielinski, M. Ficek, A. Franczak, R. Bogdanowicz, K. Darowicki, Heterogeneous oxidation of highly boron-doped diamond

[93] electrodes and its influence on the surface distribution of electrochemical activity, Electrochim. Acta 297 (2019) 1018–1027, https://doi.org/10.1016/j.electacta.2018.12.050.

[93] H. Zanin, P.W. May, D.J. Fermin, D. Plana, S.M.C. Vieira, W.I. Milne, E.J. Corat, Porous boron-doped diamond/carbon nanotube electrodes, ACS Appl. Mater. Interfaces 6 (2014) 990–995, https://doi.org/10.1021/am4044344.

[94] J.N. Soderberg, A.C. Co, A.H.C. Sirk, V.I. Birss, Impact of porous electrode properties on the electrochemical transfer coefficient, J. Phys. Chem. B 110 (2006) 10401–10410, https://doi.org/10.1021/jp060372f.

[95] A.C. Co, S.J. Xia, V.I. Birss, A kinetic study of the oxygen reduction reaction at LaSrMnO3-YSZ composite electrodes, J. Electrochem. Soc. 152 (2005) A570, https://doi.org/10.1149/1.1859612.

[96] W. Lizhang, Y. Shengxiang, W. Bo, L. Peng, L. Zhe'nan, Z. Yuemin, The influence of anode materials on the kinetics toward electrochemical oxidation of phenol, Electrochim. Acta 206 (2016) 270–277, https://doi.org/10.1016/j.electacta.2016.04.168.

[97] J.J. Warren, T.A. Tronic, J.M. Mayer, Thermochemistry of proton-coupled electron transfer reagents and its implications, Chem. Rev. 110 (2010) 6961–7001, https://doi.org/10.1021/cr100085k.

[98] D.A. Armstrong, R.E. Huie, W.H. Koppenol, S.V. Lymar, G. Merényi, P. Neta, B. Ruscic, D.M. Stanbury, S. Steenken, P. Wardman, Standard electrode potentials involving radicals in aqueous solution: inorganic radicals (IUPAC technical report), Pure Appl. Chem. 87 (2015) 1139–1150, https://doi.org/10.1515/pac-2014-0502.

[99] D.M. Stanbury, Reduction potentials involving inorganic free radicals in aqueous solution, in: A.G. Sykes (Ed.), Advances in Inorganic Chemistry, Academic Press, 1989, pp. 69–138, https://doi.org/10.1016/S0898-8838(08)60199-4.

[100] C.A. Martínez-Huitle, S. Ferro, Electrochemical oxidation of organic pollutants for the wastewater treatment: direct and indirect processes, Chem. Soc. Rev. 35 (2006) 1324–1340, https://doi.org/10.1039/B517632H.

[101] A. Hájková, J. Barek, V. Vyskočil, Electrochemical DNA biosensor for detection of DNA damage induced by hydroxyl radicals, Bioelectrochemistry 116 (2017) 1–9, https://doi.org/10.1016/j.bioelechem.2017.02.003.

[102] Y. Yi, G. Weinberg, M. Prenzel, M. Greiner, S. Heumann, S. Becker, R. Schlögl, Electrochemical corrosion of a glassy carbon electrode, Catal. Today 295 (2017) 32–40, https://doi.org/10.1016/j.cattod.2017.07.013.

[103] B.-T. Zhang, L.-X. Zhao, J.-M. Lin, Study on superoxide and hydroxyl radicals generated in indirect electrochemical oxidation by chemiluminescence and UV-visible spectra, J. Environ. Sci. 20 (2008) 1006–1011, https://doi.org/10.1016/S1001-0742(08)62200-7.

[104] F. Escalona-Durán, D. Ribeiro da Silva, C.A. Martínez-Huitle, P. Villegas-Guzman, The synergic persulfate-sodium dodecyl sulfate effect during the electro-oxidation of caffeine using active and non-active anodes, Chemosphere 253 (2020), 126599, https://doi.org/10.1016/j.chemosphere.2020.126599.

[105] M. Pierpaoli, M. Ficek, P. Jakóbczyk, J. Karczewski, R. Bogdanowicz, Self-assembly of vertically orientated graphene nanostructures: multivariate characterisation by Minkowski functionals and fractal geometry, Acta Mater. 214 (2021), 116989, https://doi.org/10.1016/j.actamat.2021.116989.

[106] Y. Einaga, Diamond electrodes for electrochemical analysis, J. Appl. Electrochem. 40 (2010) 1807–1816, https://doi.org/10.1007/s10800-010-0112-z.

[107] E. Mousset, Interest of micro-reactors for the implementation of advanced electrocatalytic oxidation with boron-doped diamond anode for wastewater treatment, Curr. Opin. Electrochem. 32 (2022), 100897, https://doi.org/10.1016/j.coelec.2021.100897.

[108] M. Qutob, M.A. Hussein, K.A. Alamry, M. Rafatullah, A review on the degradation of acetaminophen by advanced oxidation process: pathway, by-products, biotoxicity, and density functional theory calculation, RSC Adv. 12 (2022) 18373–18396, https://doi.org/10.1039/D2RA02469A.

[109] K. Waterston, J.W. Wang, D. Bejan, N.J. Bunce, Electrochemical waste water treatment: electrooxidation of acetaminophen, J. Appl. Electrochem. 36 (2006) 227–232, https://doi.org/10.1007/s10800-005-9049-z.

[115] S. Garcia-Segura, E. Brillas, Mineralization of the recalcitrant oxalic and oxamic acids by electrochemical advanced oxidation processes using a boron-doped diamond anode, Water Res. 45 (2011) 2975–2984, https://doi.org/10.1016/j.watres.2011.03.017.

[116] Y. He, X. Wang, W. Huang, R. Chen, W. Zhang, H. Li, H. Lin, Hydrophobic networked PbO2 electrode for electrochemical oxidation of paracetamol drug and degradation mechanism kinetics, Chemosphere 193 (2018) 89–99, https://doi.org/10.1016/j.chemosphere.2017.10.144.

[120] D. Miao, Z. Li, Y. Chen, G. Liu, Z. Deng, Y. Yu, S. Li, K. Zhou, L. Ma, Q. Wei, Preparation of macro-porous 3D boron-doped diamond electrode with surface micro structure regulation to enhance electrochemical degradation performance, Chem. Eng. J. 429 (2022), 132366, https://doi.org/10.1016/j.cej.2021.132366.